Journal of Electronic Materials (2024) 53:5904–5915
https://doi.org/10.1007/s11664-024-11070-4

28TH INTERNATIONAL CONFERENCE ON NUCLEAR TRACKS AND RADIATION MEASUREMENTS

Investigation of the Structural and Optical Properties of g-C_3N_4/ZrO_2 Nanocomposites

Manas Nasit[1] · Ankush Vij[2] · Rajesh Kumar[3] · Ranjeet Kumar Brajpuriya[1] · Saurabh Dalela[4] · Parvez A. Alvi[5] · Shalendra Kumar[1]

Received: 8 February 2024 / Accepted: 22 March 2024 / Published online: 22 April 2024

Abstract

This study used ultrasonication method to prepare graphitic carbon nitride (g-C_3N_4)/zirconium oxide (ZrO_2) nanocomposites with varying ratios. Various approaches were used to characterize the as-prepared nanocomposites. The structural properties were investigated by x-ray diffraction (XRD) and Fourier transform infrared (FT-IR) spectroscopy. XRD patterns showed that pure g-C_3N_4 has a unique peak, while ZrO_2 has a monoclinic phase with no additional phases. The nanocomposites exhibited peaks from both materials, indicating the successful synthesis of the nanocomposites. The optical properties of the nanocomposites were studied using UV–Vis diffuse reflectance spectroscopy (DRS) and photoluminescence spectroscopy. According to Tauc's plot, the nanocomposites g-C_3N_4:ZrO_2{1:0.5} (CZ1) and g-C_3N_4:ZrO_2{1:2} (CZ2) showed bandgaps of 2.92 eV and 2.93 eV, respectively. The photoluminescence emission of the nanocomposites displayed a broad peak centered at ~ 450 nm. According to the CIE diagram, the nanocomposites exhibited strong emission in the blue region, with 80.4% purity. The average lifetime decay times of the nanocomposites were 0.18 ms and 0.01 ms. Based on these findings, it can be concluded that this material has the potential for use in the field of optoelectronics.

Keywords g-C_3N_4/ZrO_2 · nanocomposite · XRD · UV–Vis spectroscopy · photoluminescence spectroscopy

Introduction

Over the last few years, two-dimensional (2D) materials have attracted researchers' interest because of their remarkable properties, such as mechanical qualities, high thermal conductivity, biocompatibility, and large surface area. These characteristics make 2D nanomaterials extremely useful for various applications, including sensors, photocatalysis, optoelectronics, energy storage devices, electronics, and water purification.[1,2] Numerous 2D nanomaterials have been successfully synthesized and extensively studied for their structural and optical properties, including graphene, MXenes, transition metal dichalcogenides (TMDs), black phosphorous (BP), hexagonal boron nitride (h-BN), and graphitic carbon nitride (g-C_3N_4). They have all shown a sheet-like structure with lateral sizes that can reach micrometers or greater and a thickness of only one or a few atomic layers. Due to the atomic thickness, extreme anisotropy, and electron confinement in two dimensions, 2D nanomaterials have incredibly intriguing physical, chemical, electrical, and optical features that have sparked much interest in

✉ Ankush Vij
ankush82@gmail.com

✉ Shalendra Kumar
shailuphy@gmail.com

1 Department of Physics, School of Advanced Engineering, UPES, Dehradun 248007, India

2 Department of Physics and Astrophysics, Central University of Haryana, Mahendragarh, Haryana 123029, India

3 University School of Basic and Applied Sciences, Guru Gobind Singh Indraprastha University, New Delhi 110078, India

4 Department of Pure and Applied Physics, University of Kota, Kota, Rajasthan 324005, India

5 Department of Physical Science, Banasthali Vidyapith, Banasthali, Rajasthan 304022, India

their study.[2–4] Because of the tunability of the large surface area and remarkable properties, 2D nanomaterials are critical components in developing next-generation technologies, including multidisciplinary research endeavors.

Among semiconducting 2D materials, graphitic carbon nitride (g-C_3N_4) has piqued the interest of researchers in recent decades because of its unique properties and wide range of applications in luminescence,[5] photocatalysis,[6] electrocatalysis,[7] and optoelectronics.[8] The g-C_3N_4 is a 2D semiconductor material of the carbon nitride family with a bandgap around 2.7–2.9 eV. g-C_3N_4 is thermally (up to 600–800°C) and chemically stable and has a wide surface area, which provides many sites for catalytic and electrochemical reactions. It is also an excellent electron donor and acceptor, with an appropriate bandgap for absorbing visible light, making it a promising photocatalyst for solar-powered applications.[9] Additionally, because g-C_3N_4 is composed of earth-abundant elements and does not contain harmful heavy metals, it is environmentally friendly. g-C_3N_4 comprises layers consisting of nitrogen (N) and carbon (C) atoms organized in a hexagonal lattice, just like graphite. Tri-s-triazine rings connected by carbon–nitrogen (C–N) linkages make up the fundamental repeating unit, creating a honeycomb-like structure. g-C_3N_4 has tunable photoluminescence.[10] It is suitable for environmental remediation and water purification because it generates reactive oxygen species (ROS) and breaks down organic contaminants in photocatalysis when exposed to visible light. It has also been shown to have a high level of catalytic activity when used as a co-catalyst in electrocatalysis for hydrogen evolution reaction (HER) and oxygen reduction reaction (ORR). In addition, g-C_3N_4 is used in batteries and supercapacitors. It has also been manufactured for optoelectronic devices, including sensors and photovoltaics, because of its semiconducting qualities and light-absorbing capabilities.[11–13]

The properties of graphitic carbon nitride have been enhanced via doping. The concept behind nanocomposites is based on the layered nature of g-C_3N_4 and its potential for heteroatom housing in its pores, which causes an upshift of the conduction band without obstructing the absorption of visible light.[14] Combining two-dimensional g-C_3N_4 with transition metal oxides (TMOs) yields an array of morphological features that enhance both the specific surface area and dispersion of TMOs and g-C_3N_4, which makes these combinations desirable for applications such as photocatalysis and high-specific-capacitance supercapacitors.[15] TMOs are abundant in nature and generally inexpensive, with various crystal forms including hematite, perovskite, and spinel. TMOs can exhibit a variety of shapes, ranging from zero-dimensional (0D) to 3D, which is advantageous for increasing the exposed active catalytic sites and specific surface area.[16,17] Therefore, g-C_3N_4-TMO-based nanocomposites were selected for tuning the bandgap, improving photochemical stability, and reducing charge recombination. The addition of several TMOs, including titanium oxide (TiO_2), zinc oxide (ZnO), tungsten oxide (WO_3), iron oxide (Fe_2O_3), and tin oxide (SnO_2), can enhance the photocatalytic effectiveness of g-C_3N_4[18–24] by reducing electron–hole recombination and increasing charge carrier separation. In context with this, nanocomposites of TMO-based g-C_3N_4 can be applied in a wide range of applications, with improved optical, magnetic, photocatalytic, and electrical properties, including hydrogen generation, solar cells, degradation of dyes (organic and inorganic), carbon dioxide reduction, nitrogen oxide oxidation, elimination of hazardous metals from water, especially Cr(VI), disinfection of antibodies, and sensing.[9,14,25] Liu at el. synthesized g-C_3N_4 and zinc oxide nanocomposites, which showed higher degradation efficiency for methylene blue (MB) dye than pristine g-C_3N_4.[26] He et al. fabricated a g-C_3N_4 and bismuth oxide nanocomposite by in situ synthesis at room temperature, which outperformed pure bismuth oxide and graphitic carbon nitride in terms of photocatalytic activity for phenol degradation in visible light.[27] WO_3/g-C_3N_4 prepared via co-calcination by Liang et al. showed 99.18% degradation of rhodamine B dye.[28] SnO_2 nanosheets/g-C_3N_4 produced by Vo et al. exhibited better cycling performance than standalone SnO_2 nanosheets, which is explained by the presence of g-C_3N_4.[29]

Among all the TMOs, zirconium oxide (ZrO_2) has drawn the attention of researchers in the last few years.[30–32] Zirconia is a white crystalline oxide and is among the ceramic materials that have been studied the most. ZrO_2 has unique properties including high mechanical resistance, high-temperature resistance, low thermal conductivity, and chemical resistivity. It is used in many application fields, including ceramics, biomedical implantation, refractory purposes, fuel cells, shielding with a thermal barrier, and dental implants.[33,34] ZrO_2 is a metallic oxide semiconductor substance with a large bandgap and an optical bandgap of greater than 4 eV that can be utilized to create a heterostructure with g-C_3N_4.

A few research groups have reported work on g-C_3N_4:ZrO_2.[35–37] Therefore, in this work, we synthesized g-C_3N_4 and ZrO_2 nanocomposites to improve their physical and chemical properties for optoelectronics applications. The g-C_3N_4:ZrO_2 nanocomposites were prepared using a simple ultrasonication technique. The structural properties of these nanocomposites were investigated by x-ray diffraction. The surface functional groups of the produced samples were observed using FT-IR spectroscopy, and the optical properties of the composites were characterized by UV–Vis and photoluminescence spectroscopy.

Experimental Section

Experimental Reagents

Urea (MW 60.06 g/mol; Molychem, 99% pure), zirconyl nitrate (MW 231.23 g/mol; Otto Chemie, 99.5% pure), ethanol (99.9%), and distilled water were used in the experiments. All chemicals were of analytical grade and used exactly as received.

Synthesis of Graphitic Carbon Nitride (g-C_3N_4)

Graphitic carbon nitride was synthesized by the direct heating method.[38] Urea was used as a precursor for graphitic carbon nitride. In the direct heating method, 10 g urea was placed in a silica crucible with lid to prevent degradation. Next, a muffle furnace was used to heat the silica crucible to 550°C with a 5°C ramp-up temperature. Subsequent cooling to room temperature yielded a lightweight powder with a pale yellow color. The powder was ground and used for further synthesis and characterization. This sample was designated as g-C_3N_4.

Synthesis of Zirconium Oxide

ZrO_2 was synthesized via the combustion method,[31] ZrO_2 using zirconyl nitrate ($ZrO(NO_3)_2{\cdot}H_2O$) as oxidizer and urea ($CO(NH_2)_2$) as fuel. A total of 2.309 g zirconyl nitrate and 1 g urea were mixed in stoichiometric ratios in 50 mL DI water. The mixed solution was then placed into a muffle furnace at 550°C with a ramp rate of 5°C/min for 1 h. This solution ignited in the muffle, and porous and fluffy powder was obtained. This powder was finely ground with mortar and pestle. The sample was then annealed in the furnace for 3 h at 900°C with a ramp rate of 8°C/min to produce nanoparticles for additional synthesis and characterization. This sample was designated as ZrO_2.

Synthesis of g-C_3N_4/ZrO_2 Nanocomposite

Two solutions were prepared for nanocomposite by dissolving g-C_3N_4 and ZrO_2 in double-distilled water. Each solution was stirred for 30 min using a magnetic stirrer, and then they were mixed under continued stirring for 2 h at 500 rpm. Next, the solution was sonicated for 3 h at room temperature, after which it was centrifuged, washed with ethanol and DI water, then dried overnight at 80°C. The resulting powder was finely ground with a pestle and mortar. Figure 1 shows a schematic of the synthesis. Nanocomposites of g-C_3N_4 and ZrO_2 were synthesized in two different ratios, 1:0.5 and 1:2. Nanocomposites g-C_3N_4:ZrO_2 (1:0.5) and g-C_3N_4:ZrO_2 (1:2) were designated as CZ1 and CZ2, respectively.

Instrumentation and Characterization

X-ray diffraction was carried out using a Bruker D8 Advance Eco Pro x-ray diffractometer, and the XRD pattern was then used to assess the crystal structure and determine the phase of the powder samples. To record XRD, a Cu Kα

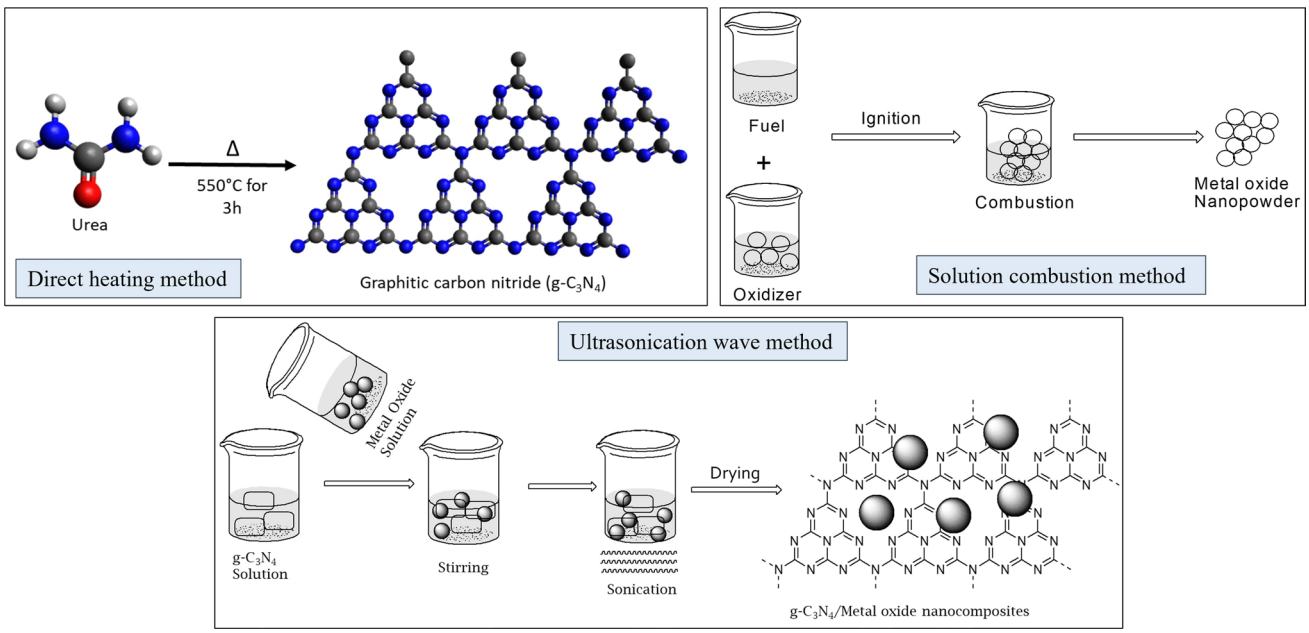

Fig. 1 Schematic diagram of ZrO_2, g-C_3N_4, CZ1, and CZ2 synthesis.

($\lambda = 1.54056$ Å) source was employed. Fourier transform infrared spectroscopy (FT-IR) was performed using a PerkinElmer FT-IR spectrometer to capture the materials' FT-IR spectra. The photoluminescence emission of samples was measured using a Horiba FluoroMax Plus spectrometer and a xenon lamp as the source. A RIMS UV–Vis diffuse reflectance spectrometer (DRS) was used to measure optical characteristics, using deuterium and halogen lamps as the sources.

Results and Discussion

XRD Analysis

Figure 2 indicates the X-ray diffraction patterns of g-C_3N_4, ZrO_2, CZ1, and CZ2. The peaks present in the XRD pattern at positions ~ 13.10° and 27.20° correspond to the (100) and (002) planes, respectively, which clearly matches with JCPDS card number 87-1526 of g-C_3N_4.[38] The diffraction peak found at ~ 13.10° is attributed to the (100) plane, which is related to the in-plane structural stacking of heptazine units with an interplanar distance of 0.686 nm. In comparison, the standard predominant peak of about 27.20° allocated to the (002) plane belongs to the inter-layer stacking of the conjugated aromatic structures with an interplanar distance of 0.332 nm.[39,40] The interplanar distance is calculated using Bragg's law (Eq. 1).[41]

$$n\lambda = 2d \cdot \sin\theta, \tag{1}$$

where n is a number of orders, the wavelength of the X-ray is indicated with λ, the incidence angle is represented with θ, and d is the interplanar distance. The ZrO_2 diffraction peaks correspond to JCPDS card number 86-1451 and it shows the monoclinic phase of ZrO_2 with P 1 21/c1 space group.[42] The crystalline size of monoclinic ZrO_2 is 40.8 nm. Average crystalline size is measured using the Debye-Scherrer formula (Eq. 2),[43]

$$D(\text{Crystalline size}) = \frac{K\lambda}{\beta\cos\theta}, \tag{2}$$

in which β indicates the full width at half maximum (FWHM) of a peak, λ is the wavelength of the X-ray, θ represents the angle of incidence, and K denotes the dimensionless shape factor, which has a value of 0.9. The XRD patterns of CZ1 and CZ2 nanocomposites show the characteristic peaks of g-C_3N_4 and ZrO_2 materials. No changes in characteristic peaks were observed for the nanocomposite sample. In nanocomposite, g-C_3N_4 peaks at 13.10° and 27.2°, and ZrO_2 has a monoclinic phase. Zhang et al. prepared g-C_3N_4:ZrO_2 which showed the same result as ours.[44] Individually, g-C_3N_4 has lower peak intensity than ZrO_2. As a result, the g-C_3N_4 peak in the XRD pattern of the nanocomposite is smaller than the ZrO_2 peak. In CZ1 the intensity of the g-C_3N_4 Characteristic peak is higher than CZ2 because CZ2 has a higher amount of ZrO_2 than CZ1. Because in nanocomposites, both g-C_3N_4 and ZrO_2 are in identical phases, they are not incorporated into each other, but instead create a heterostructure. When we compare the XRD intensity of pristine g-C_3N_4 to ZrO_2, ZrO_2 has a higher XRD intensity. As the quantity of ZrO_2 in CZ2 nanocomposites is greater than that of g-C_3N_4, the ZrO_2 peak is higher and the g-C_3N_4 peak is lower.[44]

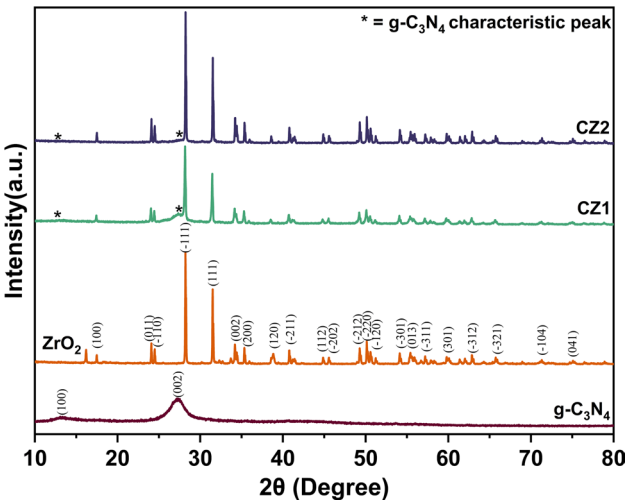

Fig. 2 X-ray diffraction patterns of g-C_3N_4, ZrO_2, CZ1, and CZ2.

FT-IR Analysis

The FT-IR spectra of g-C_3N_4, ZrO_2, CZ1, and CZ2 were examined for the presence of the functional groups, and their corresponding image is shown in Fig. 3. A strong peak in pure g-C_3N_4 at 810 cm^{-1} indicates the bending vibration of heptazine (tri-s-triazine) units. A broad peak at 2900–3600 cm^{-1} is attributed to the stretching vibration of the amino groups (N–H) of the g-C_3N_4 tri-s-triazine rings, as well as the hydroxyl group (O–H) of the adsorbed H_2O molecule. Aromatic heterocycle stretching vibrations of carbon and nitrogen (C–N and C=N) cause many intense bands in the 1240–1640 cm^{-1} range.[45] In pure ZrO_2, the absorption peaks at 508 cm^{-1}, 589 cm^{-1}, and 753 cm^{-1} correspond to the stretching vibration of Zr–O, whereas the wideband at 3445 cm^{-1} is attributed to the hydroxyl group (–OH).[46] CZ1 and CZ2 show the characteristic peaks of both g-C_3N_4 and ZrO_2 material. No changes in characteristic peaks were observed for the nanocomposite sample. Aromatic heterocycle stretching vibrations of single–double-bond carbon and nitrogen, uncondensed terminal amino groups N–H

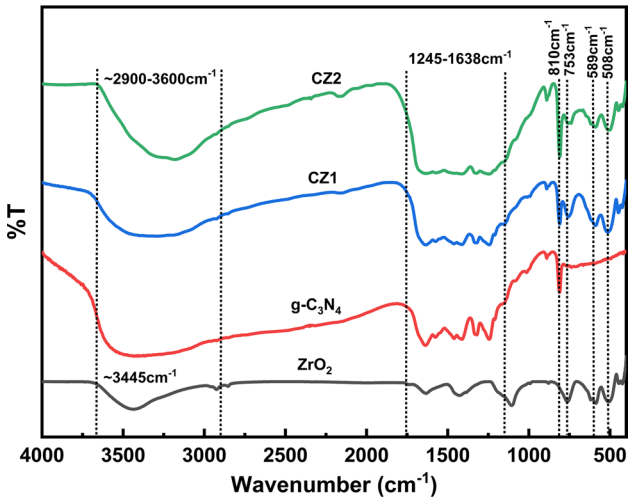

Fig. 3 FT-IR of g-C_3N_4, ZrO_2, CZ1, and CZ2.

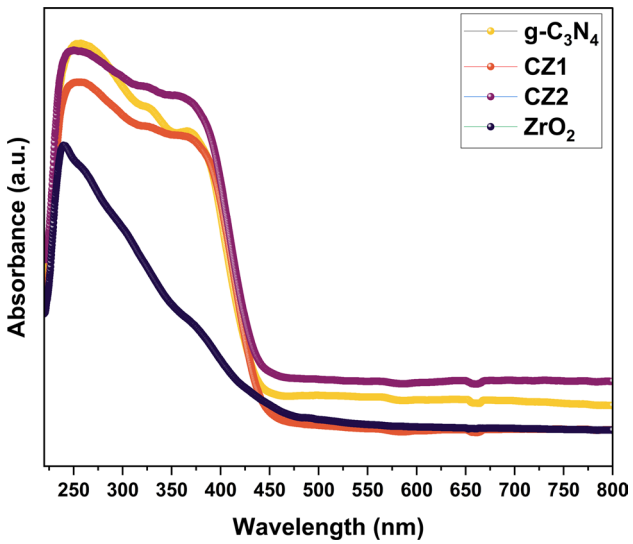

Fig. 4 Optical absorption spectrum of g-C_3N_4, ZrO_2, CZ1, and CZ2.

stretching vibration, bending vibration of heptazine rings, and stretching vibration of Zr–O remained undisturbed for the nanocomposite samples.[47] The results demonstrate that the CZ1 and CZ2 nanocomposites have a heterostructure, which agrees with the X-ray diffraction data.

UV–Vis DRS Analysis

UV–Vis DRS analysis was conducted for all samples to analyze light absorption properties. Figure 4 indicates optical absorption for g-C_3N_4, ZrO_2, CZ1, and CZ2. Bare ZrO_2 exhibits an absorption peak at 240 nm and an absorption edge near 400 nm. However, g-C_3N_4, CZ1, and CZ2 have a broad absorption peak with an absorption edge at roughly 450 nm. This is due to π–π^* electronic transition in the aromatic unit (1,3,5-triazine). A broad absorption band demonstrates significant charge transfer between g-C_3N_4 and ZrO_2.[35] When compared with pristine ZrO_2, nanocomposites show a red shift in absorption edge. This indicates that bandgap is decreased for nanocomposites. For each sample, a bandgap energy is calculated using Tauc's plot. Figure 5 shows $\alpha h\nu^2$ versus photon energy graph, which gives a direct bandgap of g-C_3N_4, ZrO_2, CZ1, and CZ2. The Tauc plot (Eq. 3) is expressed as follows:[48]

$$\alpha h\nu = A\left(h\nu - E_g\right)^m, \tag{3}$$

where E_g is the sample's bandgap energy, ν is the photon frequency, h is the Planck constant, m is a constant that varies on the electronic transition, and α is the absorption coefficient. The bandgaps of g-C_3N_4, ZrO_2, CZ1, and CZ2 are 2.95 eV, 3.4 eV, 2.92 and 2.93 eV, respectively. Because of the heterostructure between g-C_3N_4 and ZrO_2, nanocomposites have less bandgap than pure g-C_3N_4 and ZrO_2. Reduced bandgap induces absorption of light, which increases its photocatalytic activity. Equation 4 was used to calculate the g-C_3N_4, ZrO_2, CZ1, and CZ2 refractive indexes (n).[49]

$$\frac{n^2-1}{n^2+2} = 1 - \sqrt{\frac{E_g}{20}}. \tag{4}$$

The calculated values of the refractive index for g-C_3N_4, ZrO_2, CZ1, and CZ2 were 2.42, 2.42, 2.20, and 2.41, respectively. It is observed that the nanocomposites have a lower refractive index than pristine materials, which indicates that nanocomposites have a less dense structure than pristine materials.[48] Urbach energy can be used to determine the impact of all conceivable defects. It results from disorder brought on by defects, such as impurities and crystalline phase deviation, in the sample. The donor levels widen in the presence of impurities, merging with the conduction band to produce band tailing.[50] As per the Urbach rule, the absorption coefficient (α) of materials at the band edge is exponentially dependent on the energy of photons ($h\nu$), which is shown in Eq. 5.

$$\alpha = \alpha_0 \exp\left(\frac{h\nu}{E_u}\right). \tag{5}$$

Figure 6 highlights the logarithm of absorption co-efficient (ln(α)) versus photon energy graph for g-C_3N_4, ZrO_2, CZ1, and CZ2. The Urbach energy value indicates that the CZ1 and CZ2 nanocomposites have fewer lattice defects than ZrO_2. Table I shows the values of the refractive index (n), the Urbach energy (Eu), and the bandgap. The band diagram of the heterostructure of g-C_3N_4/ZrO_2 nanocomposite is shown in Fig. 7. Equations 6 and 7 represent

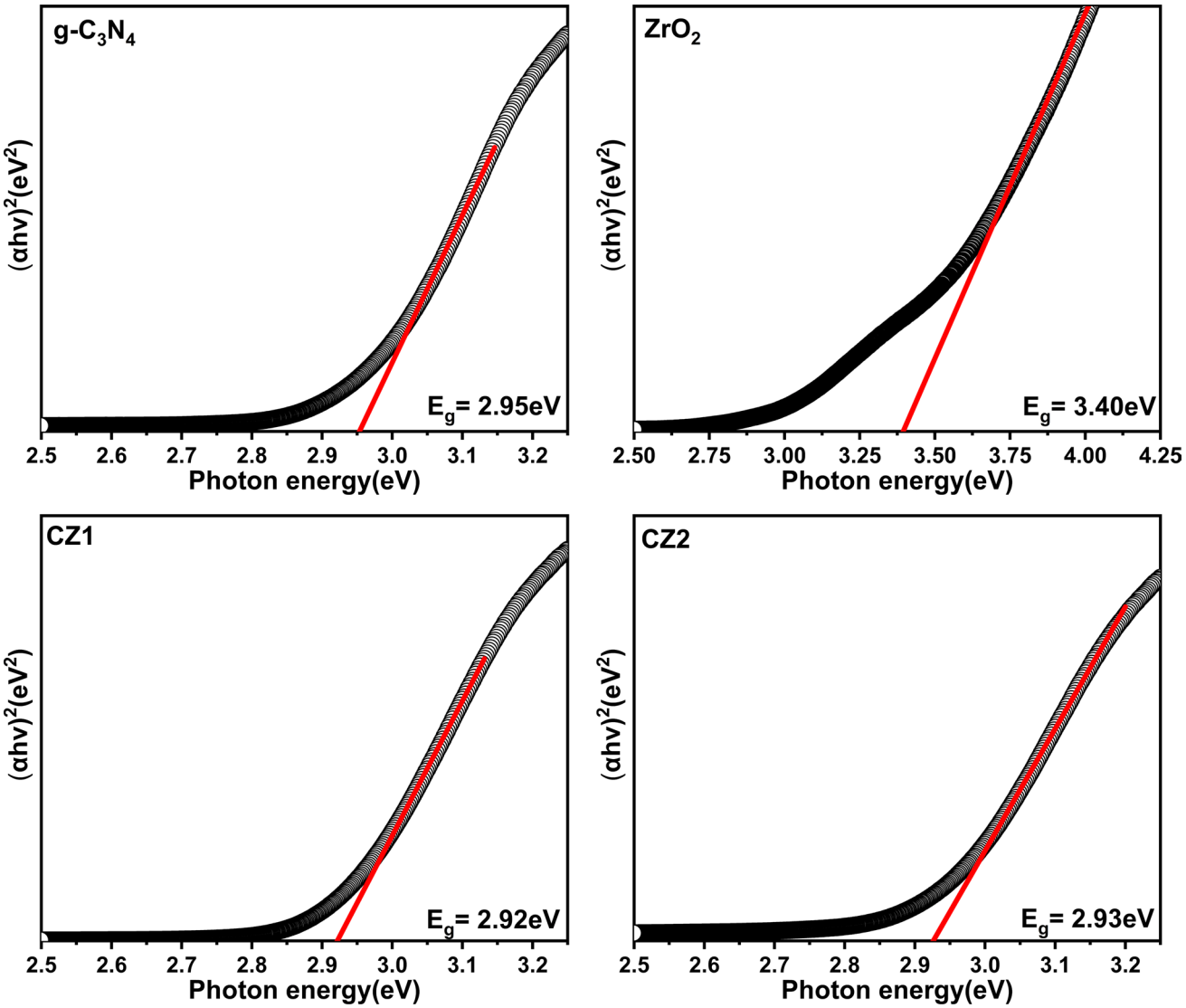

Fig. 5 Tauc plot of g-C_3N_4, ZrO_2, CZ1, and CZ2.

the relationship between the conduction band (CB) and valance band (VB) positions as determined by UV–Vis bandgap measurements.[51]

$$E_{\mathrm{VB}} = \chi - E^{c} + \left(0.5 \times E_{g}\right), \tag{6}$$

$$E_{\mathrm{CB}} = E_{\mathrm{VB}} - E_{g}, \tag{7}$$

where E_{VB} represents the energy of the valence band, and E_{CB} represents the energy of the conduction band. χ denotes the sample's electronegativity, ZrO_2 and g-C_3N_4 have electronegativity values of 5.71 eV and 4.72 eV, respectively. On the hydrogen scale, the value of free electron energy E_c is 4.5 eV. The symbol for sample bandgap energy is E_g.

Photoluminescence Spectroscopy

Figure 8 shows the photoluminescence (PL) spectrum of g-C_3N_4, CZ1, and CZ2 with an excitation of 360 nm. The inset of Fig. 8 shows the PL spectrum of ZrO_2 with an excitation of 278 nm. The PL spectra of g-C_3N_4 show a broad emission peak centered at ~ 440 nm; nanocomposites also show the same broad emission peak. The emission peak in g-C_3N_4 is caused by the electron transition from $\sigma^* \rightarrow$ LP to $\pi^* \rightarrow$ LP. The transitions from σ^* to LP and π^* to LP exhibit blue and green emission, respectively. This is analogous to the results discussed by Bauri and Chaudhary.[37] ZrO_2 shows a broad emission peak centered at 470 nm. The emission

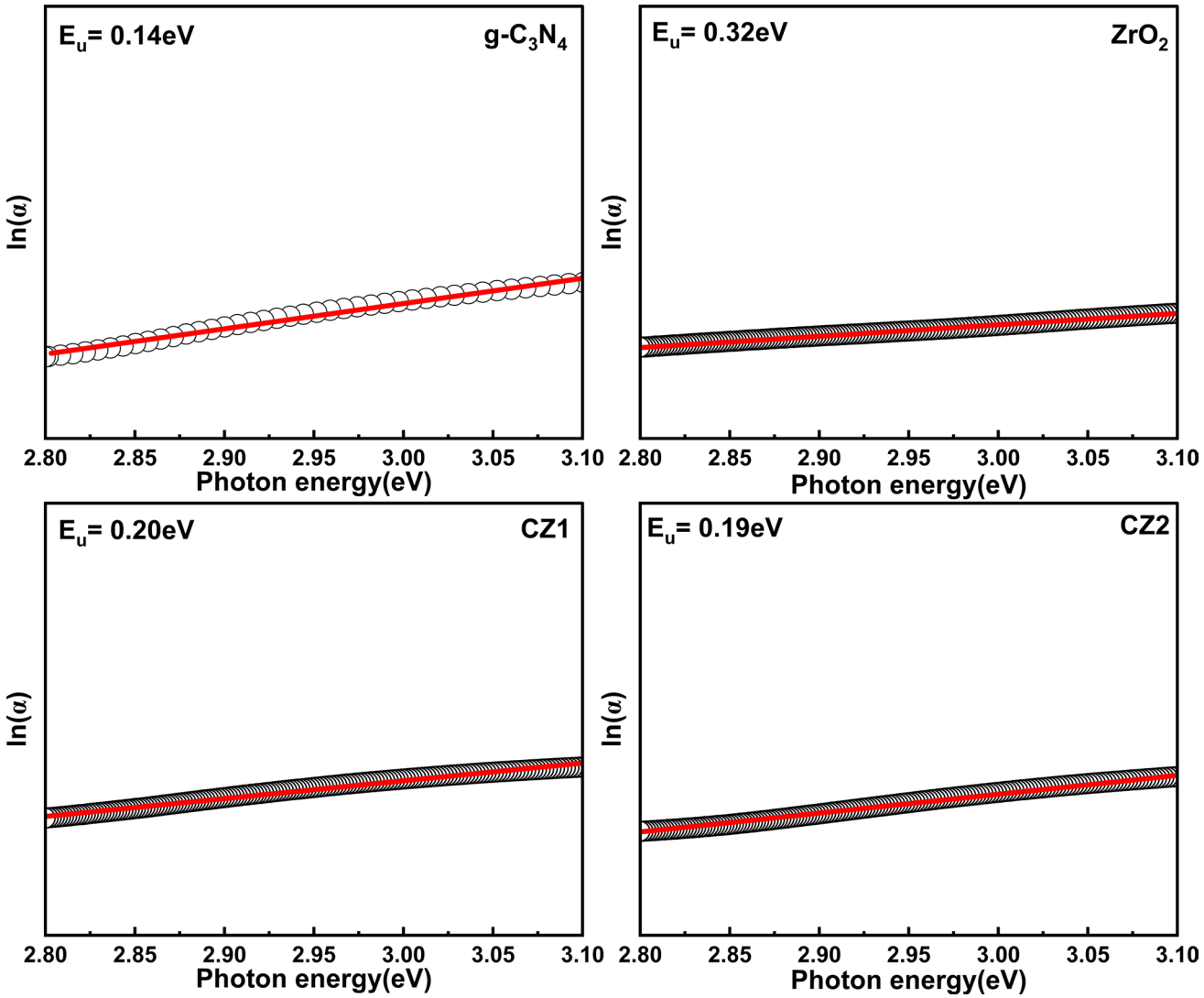

Fig. 6 Graph of ln(α) versus photon energy of g-C_3N_4, ZrO_2, CZ1, and CZ2.

Table I The values of bandgap energy (E_g), Urbach energy (E_u), and refractive index (n) of g-C_3N_4, ZrO_2, and nanocomposites

Samples	Bandgap (E_g) (eV)	Urbach energy (E_u) (eV)	Refractive index (n)
g-C_3N_4	2.95	0.14	2.42
ZrO_2	3.40	0.32	2.42
CZ1	2.92	0.20	2.20
CZ2	2.93	0.19	2.41

peaks detected at 470 nm may result from electrons being pulled in by surface defects and oxygen vacancies, which are mid-bandgap trap states.[52,53] The CZ1 and CZ2 nanocomposites show almost the same emission peak with emission position as pure g-C_3N_4, and the reason for the emission is also the same. The PL spectra of g-C_3N_4, CZ1, and CZ2 indicate that the CZ1 and CZ2 nanocomposites have lower PL intensity than pristine g-C_3N_4, which indicates the successful formation of a heterostructure between ZrO_2 and g-C_3N_4. Figure 7 depicts the band position of the g-C_3N_4/ZrO_2 nanocomposites, suggesting that electron–hole recombination is decreased and charge separation is increased in the heterostructure. The intensity of PL emission decreases as the concentration of ZrO_2 increases, demonstrating a quenching effect.[54,55]

The emission colors for all samples are specified using the 1931 CIE (x, y) color space, which is the Commission Internationale d'Eclairage (CIE) chromaticity in two-dimensional color spaces. Color components including color purity, correlated color temperature (CCT), and dominant wavelength can be determined using the CIE system. Figure 9 indicates the color coordinates of graphitic carbon nitride, zirconium oxide, and CZ1, and CZ2 nanocomposites using OSRAM

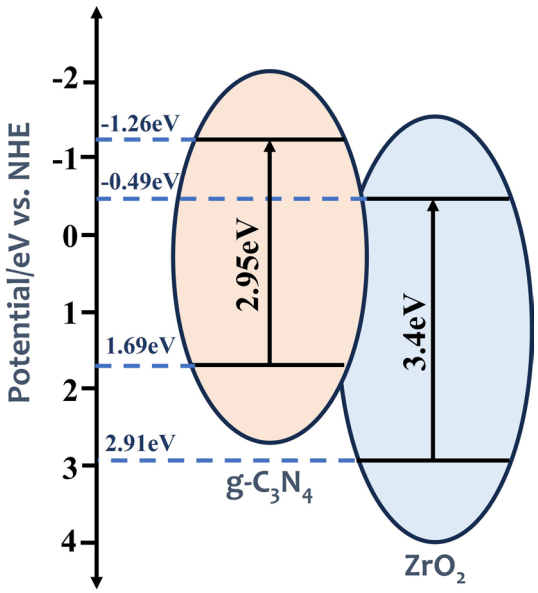

Fig. 7 Band diagram of g-C_3N_4/ZrO_2 nanocomposites.

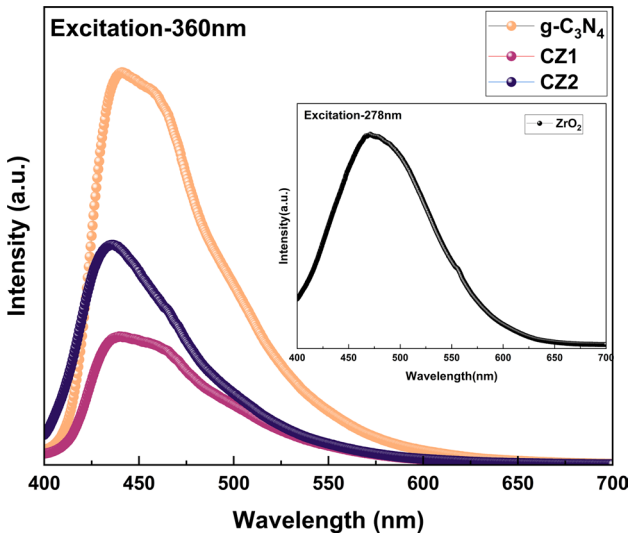

Fig. 8 Photoluminescence spectra of g-C_3N_4, CZ1, and CZ2 with excitation of 360 nm. Inset: PL of ZrO_2 with an excitation of 278 nm.

color calculator software. It can be observed that ZrO_2 presents a blue-green mixed emission with coordinates (0.19, 0.27). Blue emission is seen in g-C_3N_4, CZ1, and CZ2 at coordinates of (0.16, 0.15), (0.17, 0.15), and (0.16, 0.12), respectively. The blue emission in g-C_3N_4 and composites suggests that the transition from σ^* to LP is greater than that from π^* to LP. It also reveals a dominant wavelength and CCT of light for all samples, which is shown in Table II. The emission light in g-C_3N_4, ZrO_2, CZ1, and CZ2 shows 76.6%, 54.8%, 75%, and 80.4% purity, respectively. CZ2

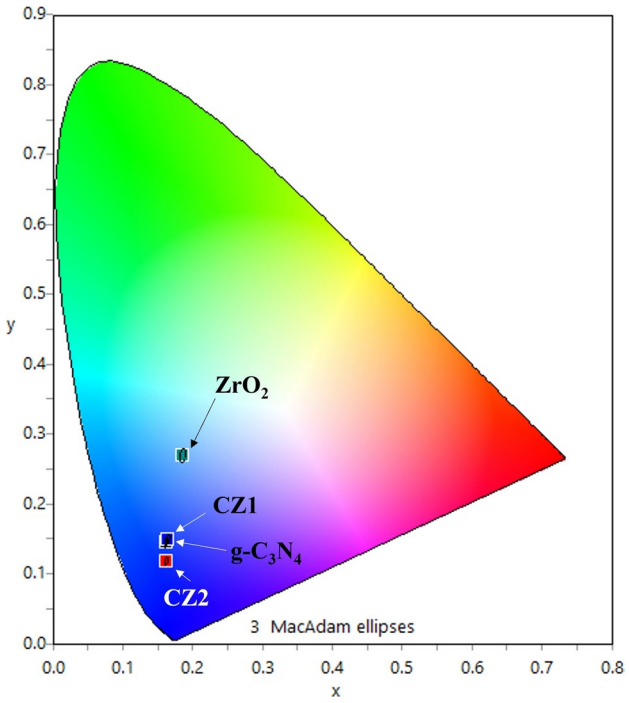

Fig. 9 Chromaticity diagram of g-C_3N_4, ZrO_2, CZ1, and CZ2.

nanocomposites have maximum purity of 80.4%. Bauri and Chaudhary conducted a similar investigation, in which the g-C_3N_4:ZrO_2 nanocomposite showed maximum purity of 53%.[37]

A luminescence decay experiment was carried out to understand better the role of emission from band-edge and trap states within the bandgap. Figure 10 shows a lifetime decay curve with the fitting of g-C_3N_4, ZrO_2, CZ1, and CZ2. The multi-exponential function Eq. 8 is used to fit these curves:[56]

$$I = \sum_{i=1,2,3\ldots} A_i \exp\left(\frac{-t}{\tau_i}\right), \tag{8}$$

where I represent PL decay intensity τ_i denotes the decay component, A_i represents the appropriate amplitude. The decay components most likely originate from the emission from exciton recombination. The long-lasting decay component might be attributed to radiative decay caused by surface-localized hole and electron recombination.[57] The tri-exponential function is used here in this work. The average decay times τ_{avg} were computed using fitting parameters and Eq. 9.[58]

$$\tau_{avg} = \frac{\sum_{i=1,2,3\ldots} A_i \tau_i^2}{\sum_{i=1,2,3\ldots} A_i \tau_i}. \tag{9}$$

Table II Value of color coordinates (x, y), dominant wavelength (λ_d), color purity, and CCT values of materials

Materials	Coordinate x	Coordinate y	Dominant wavelength (λ_d) (nm)	Color purity (%)	Correlated color temperature (CCT) (K)
g-C_3N_4	0.1620	0.1448	475	76.6	7827
ZrO_2	0.1860	0.2688	485.9	54.8	31107
CZ1	0.1652	0.1496	475.1	75.0	7676
CZ2	0.1624	0.1170	471.3	80.4	3940

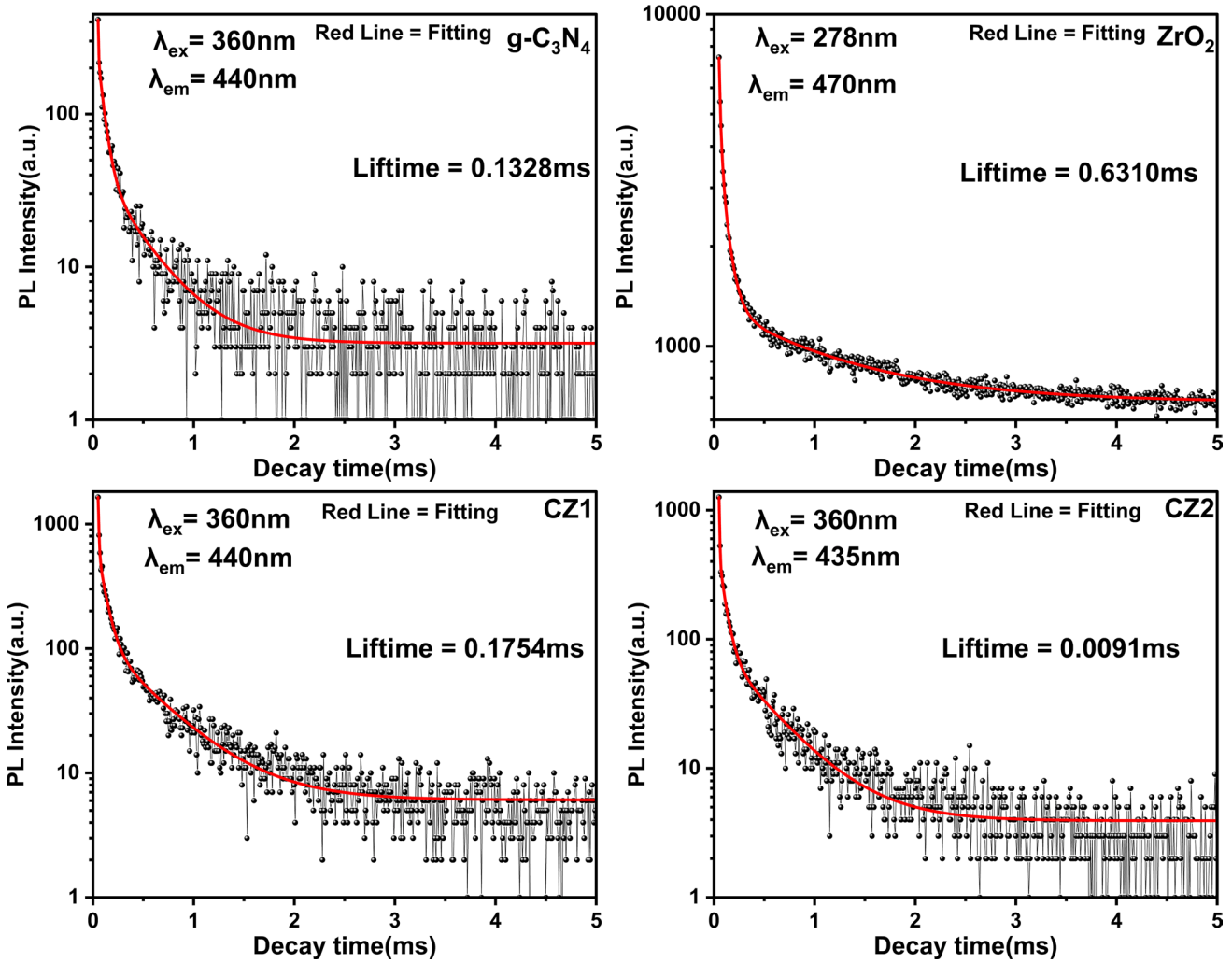

Fig. 10 Lifetime decay curves of g-C_3N_4, ZrO_2, CZ1, and CZ2.

The average lifetime decay times of g-C_3N_4, ZrO_2, CZ1, and CZ2 are 0.13 ms, 0.63 ms, 0.18 ms and 0.01 ms, respectively. ZrO_2 has a higher decay time because of the abundance of defects, such as deficiency of oxygen, the tau value is dependent upon the electrons absorbed by these defect states. These oxygen-deficient monoclinic ZrO_2 atoms act as shallow hole trappers and electron acceptors. The trapping of carriers in oxygen vacancy prevents the straight recombination of holes and electrons.[59] Also, the CZ1 and CZ2 nanocomposites have a shorter decay time than pristine ZrO_2, because the nanocomposites have decreased charge recombination, electron capture by defects or traps, and surface-localized electron–hole recombination.

Conclusion

In summary, graphitic carbon nitride was successfully prepared using the direct heating method. ZrO_2 nanoparticles were prepared using the solution combustion method. Ultrasonication methods were used to synthesize nanocomposites of g-C_3N_4 and ZrO_2. XRD and FT-IR, UV–Vis DRS, and PL spectroscopy were used for characterization. The XRD patterns and FT-IR spectra revealed the successful incorporation of ZrO_2 in g-C_3N_4 and excluded the presence of any impurity peaks. Results showed that the absorption peaks of g-C_3N_4, CZ1, and CZ2 are broad, with an absorption edge at around 450 nm. When compared to pure ZrO_2, the CZ1 and CZ2 nanocomposites exhibit a red shift in the absorption edge. This suggests that the bandgap of the CZ1 and CZ2 nanocomposites is decreased. According to Tauc's plot, the bandgaps of g-C_3N_4, ZrO_2, CZ1, and CZ2 are 2.95 eV, 3.4 eV, 2.92 eV, and 2.93 eV, respectively. The Urbach energy of the CZ1 and CZ2 nanocomposites is lower than that of pristine ZrO_2, indicating that the nanocomposites have fewer defects in the lattice than ZrO_2. The photoluminescence emission spectra show that the nanocomposites have lower photoluminescence intensity than pristine g-C_3N_4. The heterostructure of g-C_3N_4 and ZrO_2 decreases electron–hole recombination while increasing charge separation. The CIE diagram indicates that the CZ2 nanocomposites show strong blue emission, with maximum purity of 80.4%. For g-C_3N_4, ZrO_2, CZ1, and CZ2, the average lifetime decay times are 0.13 ms, 0.63 ms, 0.18 ms, and 0.01 ms, respectively. The results of this work lead us to conclude that this nanocomposite has great prospects for use in photocatalysis, as it has high charge separation and reduced electron–hole recombination.

Acknowledgements The authors are thankful to UPES, Dehradun, for funding the seed grant and to the Central Instrumentation Centre, UPES, for providing research facilities.

Conflict of interest The authors declare that none of the work presented in this study may have been influenced by any known conflicting financial interests or relationships.

References

1. A. Murali, G. Lokhande, K.A. Deo, A. Brokesh, and A.K. Gaharwar, Emerging 2D nanomaterials for biomedical applications. *Mater. Today* 50, 276–302 (2021).
2. H. Zhang, H.-M. Cheng, and P. Ye, 2D nanomaterials: beyond graphene and transition metal dichalcogenides. *Chem. Soc. Rev.* 47, 6009–6012 (2018).
3. B. Lu, Z. Zhu, B. Ma, W. Wang, R. Zhu, and J. Zhang, 2D MXene nanomaterials for versatile biomedical applications: current trends and future prospects. *Small* 17, 2100946 (2021).
4. K. Zhang, Y. Feng, F. Wang, Z. Yang, and J. Wang, Two dimensional hexagonal boron nitride (2D-hBN): synthesis, properties and applications. *J. Mater. Chem. C Mater.* 5, 11992–12022 (2017).
5. Y. Tang, H. Song, Y. Su, and Y. Lv, Turn-on persistent luminescence probe based on graphitic carbon nitride for imaging detection of biothiols in biological fluids. *Anal. Chem.* 85, 11876–11884 (2013).
6. K. Maeda, X. Wang, Y. Nishihara, D. Lu, M. Antonietti, and K. Domen, Photocatalytic activities of graphitic carbon nitride powder for water reduction and oxidation under visible light. *J. Phys. Chem. C* 113, 4940–4947 (2009).
7. J. Tian, Q. Liu, C. Ge, Z. Xing, A.M. Asiri, A.O. Al-Youbi, and X. Sun, Ultrathin graphitic carbon nitride nanosheets: a low-cost, green, and highly efficient electrocatalyst toward the reduction of hydrogen peroxide and its glucose biosensing application. *Nanoscale* 5, 8921 (2013).
8. H.Y. Hoh, Y. Zhang, Y.L. Zhong, and Q. Bao, Harnessing the potential of graphitic carbon nitride for optoelectronic applications. *Adv. Opt. Mater.* 9(16), 2100146 (2021).
9. X. Chen, Q. Liu, Q. Wu, P. Du, J. Zhu, S. Dai, and S. Yang, Incorporating graphitic carbon nitride (g-C_3N_4) quantum dots into bulk-heterojunction polymer solar cells leads to efficiency enhancement. *Adv. Funct. Mater.* 26, 1719–1728 (2016).
10. Y. Zhang, Q. Pan, G. Chai, M. Liang, G. Dong, Q. Zhang, and J. Qiu, Synthesis and luminescence mechanism of multicolor-emitting g-C_3N_4 nanopowders by low temperature thermal condensation of melamine. *Sci. Rep.* 3, 1943 (2013).
11. M.M. Taha, L.G. Ghanem, M.A. Hamza, and N.K. Allam, Highly stable supercapacitor devices based on three-dimensional bioderived carbon encapsulated g-C_3N_4 nanosheets. *ACS Appl. Energy Mater.* 4, 10344–10355 (2021).
12. W.-J. Ong, L.-L. Tan, Y.H. Ng, S.-T. Yong, and S.-P. Chai, Graphitic carbon nitride (g-C_3N_4)-based photocatalysts for artificial photosynthesis and environmental remediation: Are We a step closer to achieving sustainability? *Chem. Rev.* 116, 7159–7329 (2016).
13. F. Goettmann, A. Fischer, M. Antonietti, and A. Thomas, Metal-free catalysis of sustainable Friedel-Crafts reactions: direct activation of benzene by carbon nitrides to avoid the use of metal chlorides and halogenated compounds. *Chem. Commun.* (2006). https://doi.org/10.1039/B608532F.
14. L. Jiang, X. Yuan, Y. Pan, J. Liang, G. Zeng, Z. Wu, and H. Wang, Doping of graphitic carbon nitride for photocatalysis: a review. *Appl. Catal. B* 217, 388–406 (2017).
15. L. Bai, H. Huang, S. Yu, D. Zhang, H. Huang, and Y. Zhang, Role of transition metal oxides in g-C_3N_4-based heterojunctions for photocatalysis and supercapacitors. *J. Energy Chem.* 64, 214–235 (2022).
16. J. Meyer, S. Hamwi, M. Kröger, W. Kowalsky, T. Riedl, and A. Kahn, Transition metal oxides for organic electronics: energetics. *Device Phys. Appl. Adv. Mater.* 24, 5408–5427 (2012).
17. M.Z. Rahman, F. Raziq, H. Zhang, and J. Gascon, Key strategies for enhancing H2 production in transition metal oxide based photocatalysts. *Angew. Chem.* 135(48), e202305385 (2023).
18. K. Katsumata, R. Motoyoshi, N. Matsushita, and K. Okada, Preparation of graphitic carbon nitride (g-C_3N_4)/WO_3 composites and enhanced visible-light-driven photodegradation of acetaldehyde gas. *J. Hazard. Mater.* 260, 475–482 (2013).
19. S. Le, T. Jiang, Y. Li, Q. Zhao, Y. Li, W. Fang, and M. Gong, Highly efficient visible-light-driven mesoporous graphitic carbon nitride/ZnO nanocomposite photocatalysts. *Appl. Catal. B* 200, 601–610 (2017).
20. I. Rabani, R. Zafar, K. Subalakshmi, H.-S. Kim, C. Bathula, and Y.-S. Seo, A facile mechanochemical preparation of Co_3O_4@g-C_3N_4 for application in supercapacitors and

degradation of pollutants in water. *J. Hazard. Mater.* 407, 124360 (2021).
21. D. Yan, X. Wu, J. Pei, C. Wu, X. Wang, and H. Zhao, Construction of g-C_3N_4/TiO_2/Ag composites with enhanced visible-light photocatalytic activity and antibacterial properties. *Ceram. Int.* 46, 696–702 (2020).
22. G.R. Surikanti, P. Bajaj, and M.V. Sunkara, g-C_3N_4-mediated synthesis of Cu_2O To obtain porous composites with improved visible light photocatalytic degradation of organic dyes. *ACS Omega* 4, 17301–17316 (2019).
23. C. Chen, M. Xie, L. Kong, W. Lu, Z. Feng, and J. Zhan, Mn_3O_4 nanodots loaded g-C_3N_4 nanosheets for catalytic membrane degradation of organic contaminants. *J. Hazard. Mater.* 390, 122146 (2020).
24. A. Alaghmandfard and K. Ghandi, A comprehensive review of graphitic carbon nitride (g-C_3N_4)–metal oxide-based nanocomposites: potential for photocatalysis and sensing. *Nanomaterials* 12, 294 (2022).
25. V. Hasija, P. Raizada, P. Singh, N. Verma, A.A.P. Khan, A. Singh, R. Selvasembian, S.Y. Kim, C.M. Hussain, V.-H. Nguyen, and Q. Van Le, Progress on the photocatalytic reduction of hexavalent Cr(VI) using engineered graphitic carbon nitride. *Process Saf. Environ. Prot.* 152, 663–678 (2021).
26. L. Liu, X. Luo, Y. Li, F. Xu, Z. Gao, X. Zhang, Y. Song, H. Xu, and H. Li, Facile synthesis of few-layer g-C_3N_4/ZnO composite photocatalyst for enhancing visible light photocatalytic performance of pollutants removal. *Colloids Surf. A Physicochem. Eng. Asp.* 537, 516–523 (2018).
27. R. He, J. Zhou, H. Fu, S. Zhang, and C. Jiang, Room-temperature in situ fabrication of Bi_2O_3 /g-C_3N_4 direct Z-scheme photocatalyst with enhanced photocatalytic activity. *Appl. Surf. Sci.* 430, 273–282 (2018).
28. J. Liang, Y. Li, J. Zhang, C. Li, X. Yang, X. Chen, F. Wang, and C. Chen, Crystalline phase engineering in WO_3/g-C_3N_4 composites for improved photocatalytic performance under visible light. *Mater. Res. Express* 7, 065503 (2020).
29. V. Vo, X.D. Nguyen Thi, Y.-S. Jin, G. Ly Thi, T.T. Nguyen, T.Q. Duong, and S.-J. Kim, SnO_2 nanosheets/g-C_3N_4 composite with improved lithium storage capabilities. *Chem. Phys. Lett.* 674, 42–47 (2017).
30. SYu. Sokovnin, N. Pizurova, V.G. Ilves, P. Roupcová, M.G. Zuev, M.A. Uimin, M.V. Ulitko, and O.A. Svetlova, Properties of ZrO_2 and Ag–ZrO_2 nanopowders prepared by pulsed electron beam evaporation. *Ceram. Int.* 48, 17703–17713 (2022).
31. M. Thakur, A. Vij, A. Kumar, B.H. Koo, F. Singh, and V.S. Rangra, Electronic structure and defect-induced luminescence study of phase-stabilized t-ZrO_2 nanocrystals. *Luminescence* 38, 762–771 (2023).
32. M. Thakur, A. Vij, F. Singh, and V.S. Rangra, Spectroscopic studies of metastable tetragonal ZrO_2 nanocrystals. *Spectrochim. Acta A Mol. Biomol. Spectrosc.* 305, 123495 (2024).
33. K. Shanmugam and R. Sahadevan, Bioceramics—an introductory overview, *Fundamental Biomaterials: Ceramics*. (Elsevier, 2018), pp. 1–46.
34. S. Reyes-López, Review of the synthesis, characterization and application of zirconia mixed metal oxide nanoparticles. (2018) https://doi.org/10.5281/zenodo.1403844
35. G. Ahilandeswari and D. Arivuoli, Enhanced sunlight-driven photocatalytic activity in assembled ZrO_2/g-C_3N_4 nanocomposite. *J. Mater. Sci. Mater. Electron.* 33, 23986–24002 (2022).
36. Q. Zhang, W. Zhang, B. Liang, J. Liu, D. Lan, and M. Jiao, ZrO_2/C_3N_4 nanocomposites: green solid-state grinding synthesis, characterization, and photocatalytic degradation of MB dye. *J. Inorg. Organomet. Polym. Mater.* 32, 4434–4440 (2022).
37. J. Bauri and R.B. Choudhary, Thermal and electronic states of exfoliated gC_3N_4-based nanocomposite with ZrO_2 nanoparticles as a robust emissive layer. *Mater. Sci. Semicond. Process.* 154, 107205 (2023).
38. L. Wang, Y. Hou, S. Xiao, F. Bi, L. Zhao, Y. Li, X. Zhang, G. Gai, and X. Dong, One-step, high-yield synthesis of g-C_3N_4 nanosheets for enhanced visible light photocatalytic activity. *RSC Adv.* 9, 39304–39314 (2019).
39. X. Wang, X. Chen, A. Thomas, X. Fu, and M. Antonietti, Metal-containing carbon nitride compounds: a new functional organic-metal hybrid material. *Adv. Mater.* 21, 1609–1612 (2009).
40. X. Wang, K. Maeda, A. Thomas, K. Takanabe, G. Xin, J.M. Carlsson, K. Domen, and M. Antonietti, A metal-free polymeric photocatalyst for hydrogen production from water under visible light. *Nat. Mater.* 8, 76–80 (2009).
41. L.R.B. Elton and D.F. Jackson, X-ray diffraction and the Bragg Law. *Am. J. Phys.* 34, 1036–1038 (1966).
42. M. Ramachandran, R. Subadevi, W.-R. Liu, and M. Sivakumar, Facile synthesis and characterization of ZrO_2 nanoparticles via modified Co-precipitation method. *J. Nanosci. Nanotechnol.* 18, 368–373 (2018).
43. U. Holzwarth and N. Gibson, The Scherrer equation versus the 'Debye-Scherrer equation.' *Nat. Nanotechnol.* 6, 534–534 (2011).
44. K. Zhang, M. Zhou, C. Yu, K. Yang, X. Li, W. Dai, J. Guan, Q. Shu, and W. Huang, Construction of S-scheme g-C_3N_4/ZrO_2 heterostructures for enhancing photocatalytic disposals of pollutants and electrocatalytic hydrogen evolution. *Dyes Pigm.* 180, 108525 (2020).
45. T. Chen, W. Quan, L. Yu, Y. Hong, C. Song, M. Fan, L. Xiao, W. Gu, and W. Shi, One-step synthesis and visible-light-driven H_2 production from water splitting of Ag quantum dots/g-C_3N_4 photocatalysts. *J. Alloys Compd.* 686, 628–634 (2016).
46. R.S. Das, S.K. Warkhade, A. Kumar, and A.V. Wankhade, Graphene oxide-based zirconium oxide nanocomposite for enhanced visible light-driven photocatalytic activity. *Res. Chem. Intermed.* 45, 1689–1705 (2019).
47. M. Ismael, Y. Wu, and M. Wark, Photocatalytic activity of ZrO_2 composites with graphitic carbon nitride for hydrogen production under visible light. *New J. Chem.* 43, 4455–4462 (2019).
48. N.S. Leel, M. Kiran, M.K. Kumawat, P.A. Alvi, V.S. Vats, D. Patidar, B. Dalela, S. Kumar, and S. Dalela, Oxygen vacancy driven luminescence, ferromagnetic and electronic structure properties of Eu doped CeO_2 nanoparticles. *J. Lumin.* 263, 119981 (2023).
49. P. Nagaraju, Y. V. Kumar, M. V. R. Reddy, C. V. Reddy, V. R. Reddy, D. M. Phase, and I.-I. UGC-DAE-CSR, Preparation, Micro structural characterization and Optical characterization of pure and Gd-doped ceria thin films. *Int. J. Sci. Eng. Res.* 5, 185–190 (2014).
50. W. Bousslama, H. Elhouichet, and M. Férid, Enhanced photocatalytic activity of Fe doped ZnO nanocrystals under sunlight irradiation. *Optik (Stuttg)* 134, 88–98 (2017).
51. J. Luo, X. Zhou, L. Ma, and X. Xu, Enhancing visible-light photocatalytic activity of g-C_3N_4 by doping phosphorus and coupling with CeO_2 for the degradation of methyl orange under visible light irradiation. *RSC Adv.* 5, 68728–68735 (2015).
52. J. Liang, Z. Deng, X. Jiang, F. Li, and Y. Li, Photoluminescence of tetragonal ZrO_2 nanoparticles synthesized by microwave irradiation. *Inorg. Chem.* 41, 3602–3604 (2002).
53. K. Smits, D. Jankovica, A. Sarakovskis, and D. Millers, Up-conversion luminescence dependence on structure in zirconia nanocrystals. *Opt. Mater. (Amst.)* 35, 462–466 (2013).
54. L.-R. Zou, G.-F. Huang, D.-F. Li, J.-H. Liu, A.-L. Pan, and W.-Q. Huang, A facile and rapid route for synthesis of g-C_3N_4 nanosheets with high adsorption capacity and photocatalytic activity. *RSC Adv.* 6, 86688–86694 (2016).
55. P. Chen, P. Xing, Z. Chen, X. Hu, H. Lin, L. Zhao, and Y. He, In-situ synthesis of $AgNbO_3$/g-C_3N_4 photocatalyst via microwave

heating method for efficiently photocatalytic H_2 generation. *J. Colloid Interface Sci.* 534, 163–171 (2019).
56. H.N. Ghosh and S. Adhikari, Trap state emission from TiO_2 nanoparticles in microemulsion solutions. *Langmuir* 17, 4129–4130 (2001).
57. X. Wang, L. Qu, J. Zhang, X. Peng, and M. Xiao, Surface-related emission in highly luminescent CdSe quantum dots. *Nano Lett.* 3, 1103–1106 (2003).
58. M. Jones, J. Nedeljkovic, R.J. Ellingson, A.J. Nozik, and G. Rumbles, Photoenhancement of luminescence in colloidal CdSe quantum dot solutions. *J. Phys. Chem. B* 107, 11346–11352 (2003).
59. N.C. Horti, M.D. Kamatagi, S.K. Nataraj, M.N. Wari, and S.R. Inamdar, Structural and optical properties of zirconium oxide (ZrO_2) nanoparticles: effect of calcination temperature. *Nano Express* 1, 010022 (2020).